Isolating along-strike variations in the depth extent of shallow creep and fault locking on the northern Great Sumatran Fault

Takeo Ito,[1] Endra Gunawan,[1] Fumiaki Kimata,[1] Takao Tabei,[2] Mark Simons,[3] Irwan Meilano,[4] Agustan,[5] Yusaku Ohta,[6] Irwandi Nurdin,[7] and Didik Sugiyanto[7]

Received 18 October 2011; revised 9 May 2012; accepted 14 May 2012; published 28 June 2012.

[1] The Great Sumatran Fault system in Indonesia is a major right-lateral trench-parallel system that can be divided into several segments, most of which have ruptured within the last century. This study focuses on the northern portion of the fault system which contains a 200-km-long segment that has not experienced a major earthquake in at least 170 years. In 2005, we established the Aceh GPS Network for the Sumatran Fault System (AGNeSS) across this segment. AGNeSS observes large displacements which include significant postseismic deformation from recent large megathrust earthquakes as well as interseismic deformation due to continued elastic loading of both the megathrust and the strike slip system. We parameterize the displacements due to afterslip on the megathrust using a model based on a rate- and state-dependent friction formalism. Using this approach, we are able to separate afterslip from other contributions. We remove predicted deformation due to afterslip from the observations, and use these corrected time series to infer the depth of shallow aseismic creep and deeper locked segments for the Great Sumatran Fault. In the northern portion of this fault segment, we infer aseismic creep down to 7.3 $\pm$ 4.8 km depth at a rate of 2.0 $\pm$ 0.6 cm/year. In the southwestern portion of the segment, we estimate a locking depth of 14.8 $\pm$ 3.4 km with a downdip slip rate of 1.6 $\pm$ 0.6 cm/year. This portion of the fault is capable of producing a magnitude 7.0 earthquake.

Citation: Ito, T., E. Gunawan, F. Kimata, T. Tabei, M. Simons, I. Meilano, Agustan, Y. Ohta, I. Nurdin, and D. Sugiyanto (2012), Isolating along-strike variations in the depth extent of shallow creep and fault locking on the northern Great Sumatran Fault, *J. Geophys. Res.*, *117*, B06409, doi:10.1029/2011JB008940.

1. Introduction

[2] The Great Sumatran Fault (GSF) system in Indonesia is a major right lateral trench-parallel fault systems that accommodates a significant fraction of the strike-slip component of the oblique convergence between the Australian/Indian and Eurasian plates [*Genrich et al.*, 2000; *Sieh and Natawidjaja*, 2000]. The 1900-km-long fault system can be divided into several segments, most of which have broken within the last century in earthquakes with magnitudes between 6.0 and 7.7 (see Figure 1a). However, two segments are devoid of any record of recent earthquakes. One of these segments traverses the northwestern part of the Sumatra Island passing through the suburb of Banda Aceh city, the local capital of the Aceh Province with a population of over 260,000. The lack of major earthquakes in at least in 170 years along this 200-km-long segment suggest the potential for high seismic hazard for this region [*Bellier et al.*, 1997; *Sieh and Natawidjaja*, 2000]. Here, we focus on GPS observations of crustal deformation on this northern portion of the GSF to constrain estimates of regional seismic potential.

1.1. Previous Studies

[3] Deformation along the GSF system has been studied based on variety of geodetic and geological observations [*Bennett et al.*, 1981; *Natawidjaja and Sieh*, 1994; *Sieh et al.*, 1994; *Bellier and Sebrier*, 1995; *Sieh and Natawidjaja*, 2000]. Geologic estimates of slip rates on the GSF increase from southeast to northwest, with maximum rates estimated to reach about 3.8 cm/year in the northwestern part of the Sumatra Island (see Figure 1a) [*Bennett et al.*, 1981; *Natawidjaja and Sieh*, 1994; *Sieh et al.*, 1994; *Bellier and Sebrier*, 1995; *Sieh and Natawidjaja*, 2000].

[1]Graduate School of Environmental Studies, Nagoya University, Nagoya, Japan.
[2]Department of Applied Science, Kochi University, Akebono-cho, Japan.
[3]Seismological Laboratory, California Institute of Technology, Pasadena, California, USA.
[4]Geodesy Research Division, Bandung Institute of Technology, Bandung, Indonesia.
[5]Center of Technology for Natural Resources Inventory, BPPT, Jakarta, Indonesia.
[6]Graduate School of Science, Tohoku University, Sendai, Japan.
[7]Physics Department, Syiah Kuala University, Aceh, Indonesia.

Corresponding author: T. Ito, Graduate School of Environmental Studies, Nagoya University, D2-2 (510), Furo-cho, Chikusa-ku, Nagoya, Aichi, 464-8602, Japan. (takeo)_ito@nagoya-u.jp)

0148-0227/12/2011JB008940

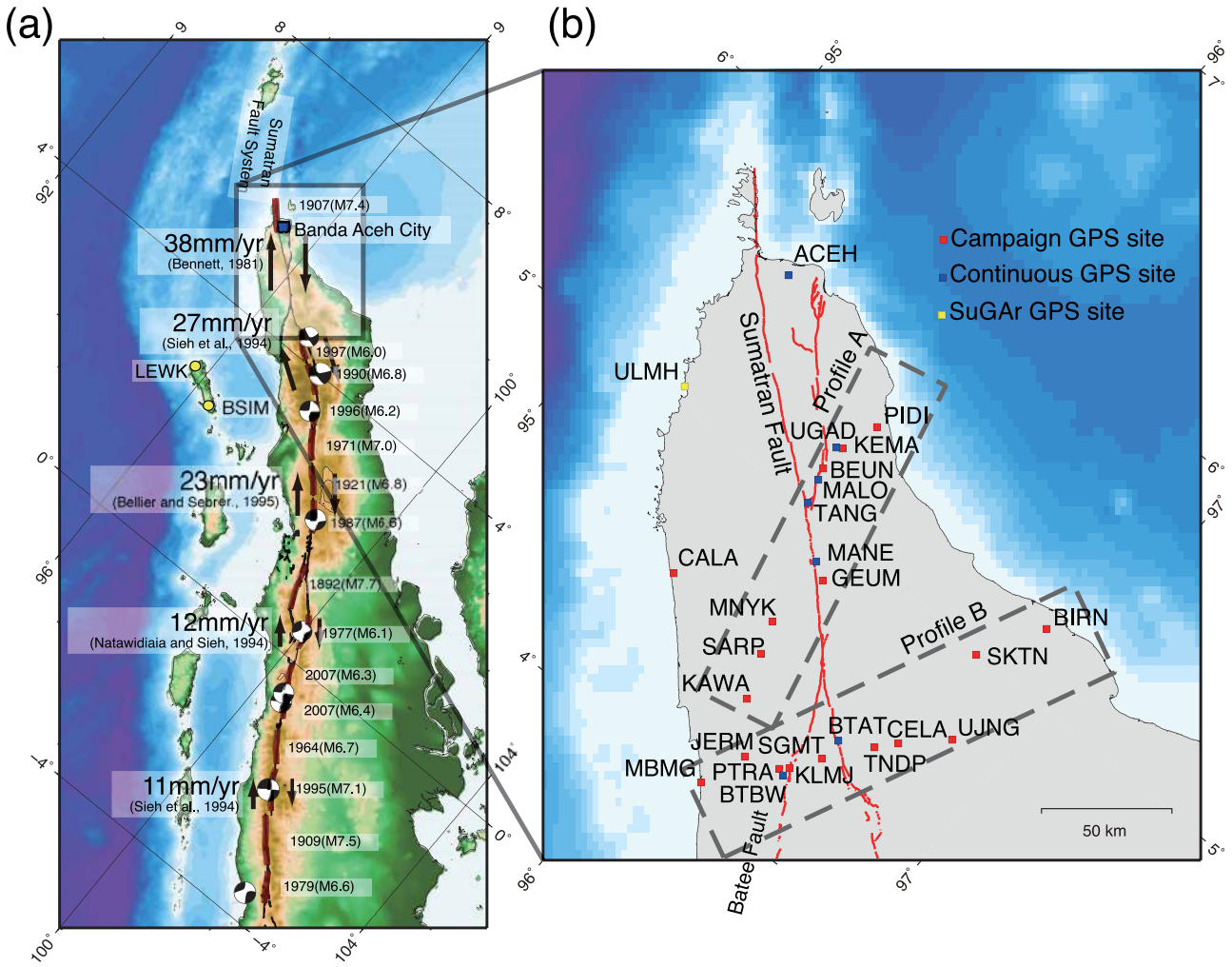

Figure 1. (a) Overview of the GSF system. Source regions of large earthquake from historical records are shown in bold red lines. Also shows are the long-term offset rates along the GSF system. Long-term offset rates are based on *Bennett et al.* [1981], *Sieh et al.* [1994], *Natawidjaja and Sieh* [1994], and *Bellier and Sebrier* [1995]. Yellow circles are GPS site belonging to Sumatran GPS Array (SuGAr) network. The gray rectangle is our study area. (b) Zoom into grayish rectangle of Figure 1a. Observation map of AGNeSS. Red, blue, and yellow squares are campaign, continuous, and SuGAr GPS sites, respectively. Red lines indicate the Sumatran and Batee faults, respectively. Rectangles with grayish broken line show profiles of GPS site.

[4] Using GPS observations, *Genrich et al.* [2000] reports estimated slip deficit rates of 2.3 $\sim$ 2.6 cm/year on the GSF between 0.8°S to 2.7°N. Estimated locking depths for the GSF between 0.8°S to 1.3°N are about 21 $\sim$ 24 km. However, around 0.6°N, the estimated locking depth was estimated to be 56 $\pm$ 35 km [*Genrich et al.*, 2000]. This region experienced a M_w = 7.8 in 1892, the largest documented event of this class on the GSF(see Figure 1a). Further north, on the GSF, between 2.2°N to 2.7°N, the locking depth is estimated to be about 9 km, significantly shallower than to the south. Moreover, for the Banda Aceh transect, the locking depth is shallower than 15 km, with an estimated slip deficit rate 0.5 $\pm$ 0.2 cm/year [*Genrich et al.*, 2000]. This estimated slip deficit rate is significantly slower than estimated geological slip rate. This discrepancy may be partially due to the complexity associated with the branching fault system in the Banda Aceh segment (see Figure 1b).

2. GPS Observations

[5] The 2004 Sumatra-Andaman earthquake (M_w 9.2) occurred at the subducting zone in the northern part of Sunda trench. GPS observations observed about 3 m of coseismic displacements in a southwesterly direction in Aceh region [*Subarya et al.*, 2006]. After the 2004 Sumatra-Andaman earthquake, we began to install a mixed continuous and campaign GPS network in northern Sumatra called the Aceh GPS Network for the Sumatran fault System (AGNeSS). AGNeSS is constructed across the northwestern segment of the GSF in Aceh province, located between 4.0°N to 5.5°N. We installed a permanent continuous GPS site on March

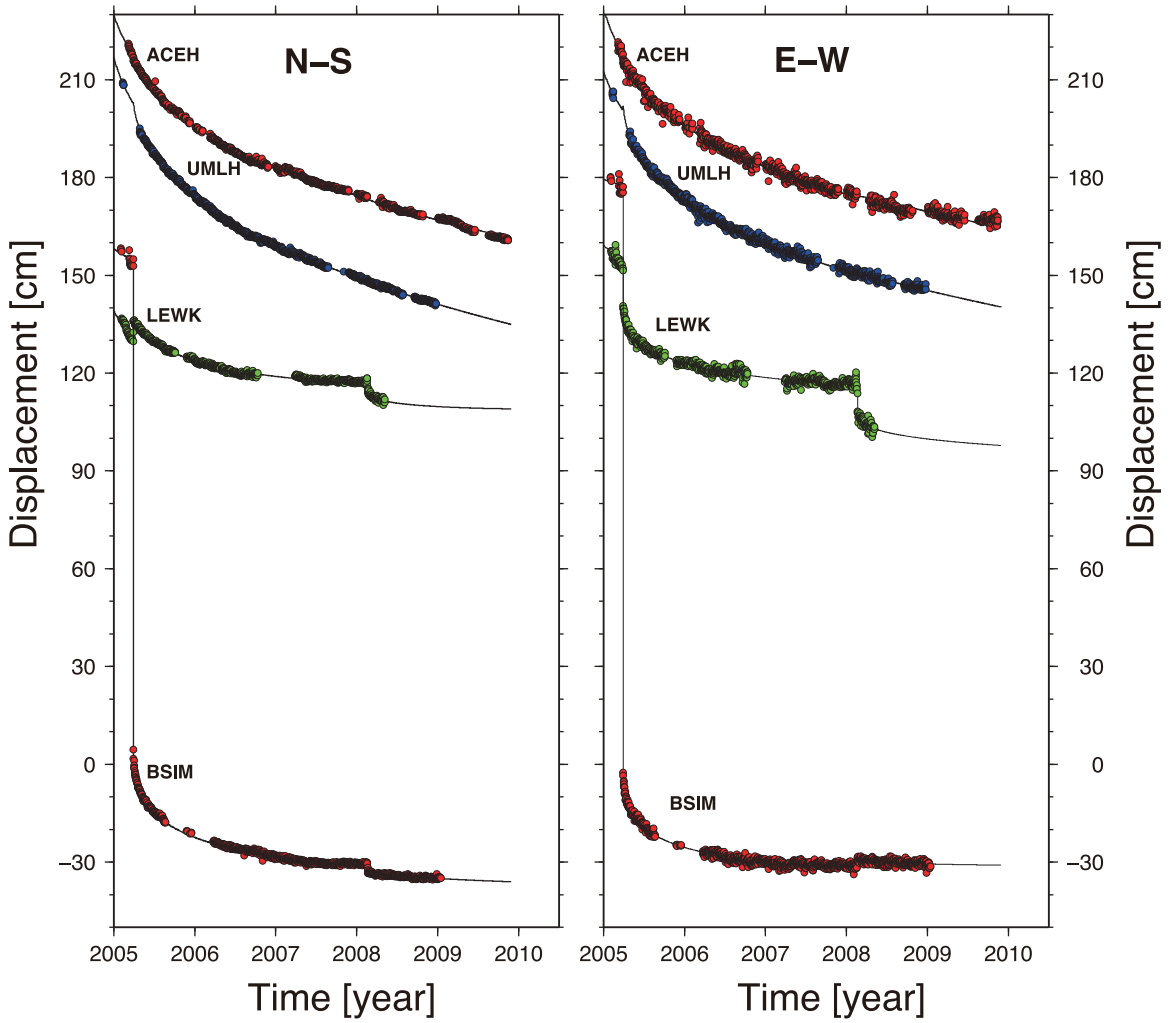

Figure 2. Time series of postseismic displacement at stations, ACEH, UMLH, LEWK, and BSIM. Locations of GPS station are shown in Figure 1b. (right) North-south and (left) east-west components. Each thin line are fitted lines using equation (1). These time series are respect to ITRF2005.

2005 in Banda Aceh city, which we have continued to operate since then. AGNeSS started with 1 continuous and 8 campaign GPS sites in November 2005, we added 4 campaign GPS sites to AGNeSS in November 2006, 5 continuous and 4 campaign GPS sites in November 2007, and 1 continuous and 3 campaign GPS sites in June 2008. AGNeSS currently consists of 7 continuous and 17 campaign GPS sites. We conducted separate campaigns in November 2005, November 2006, November 2007, June 2008, October 2008, June 2009, and November 2009.

[6] Our goal is to evaluate the seismic hazard on the northwestern part of the GSF. Therefore, we designed AGNeSS to monitor earthquake activity and to detect strain accumulation in the vicinity of the GSF (see Figure 1b). AGNeSS consists of two approximately linear profiles across the GSF, which we refer to as PA (Profile A [the northwestern profile]) and PB (Profile B [the southeastern profile]). The PA consists of 4 continuous and 7 campaign GPS sites, and the PB consists of 2 continuous and 10 campaign GPS sites. The mean fault normal distance between each GPS site in PA is less than 5 km near the fault, although GPS sites are more sparsely located on the southwestern side of the fault due to the challenge of dealing with the jungle. In general, PB is sparser than PA due to both jungle and rough terrain. See Appendix A for a description of monumentation and data reduction.

[7] Figures 2, 3, and 4 show observed displacement time series. These time series clearly show postseismic deformation due to 2004 and 2005 megathrust earthquakes. There is additional anomalous behavior in the east-west component of site TNDP. The observation period of TNDP site is only two years, the shortest in AGNeSS. Further complicating things, TNDP is located near a stream which may induce local hydrological effects. Thus, from here on out, we do not use observations from TNDP.

3. Postseismic Deformation

[8] Immediately after the 2004 Sumatra-Andaman earthquake, we established one continuous and 8 campaign GPS sites on the northern part of Sumatra Island. These sites include some of the sites that were earlier installed and occupied by BAKOSURTANAL before the earthquake. After the earthquake, large postseismic displacements toward

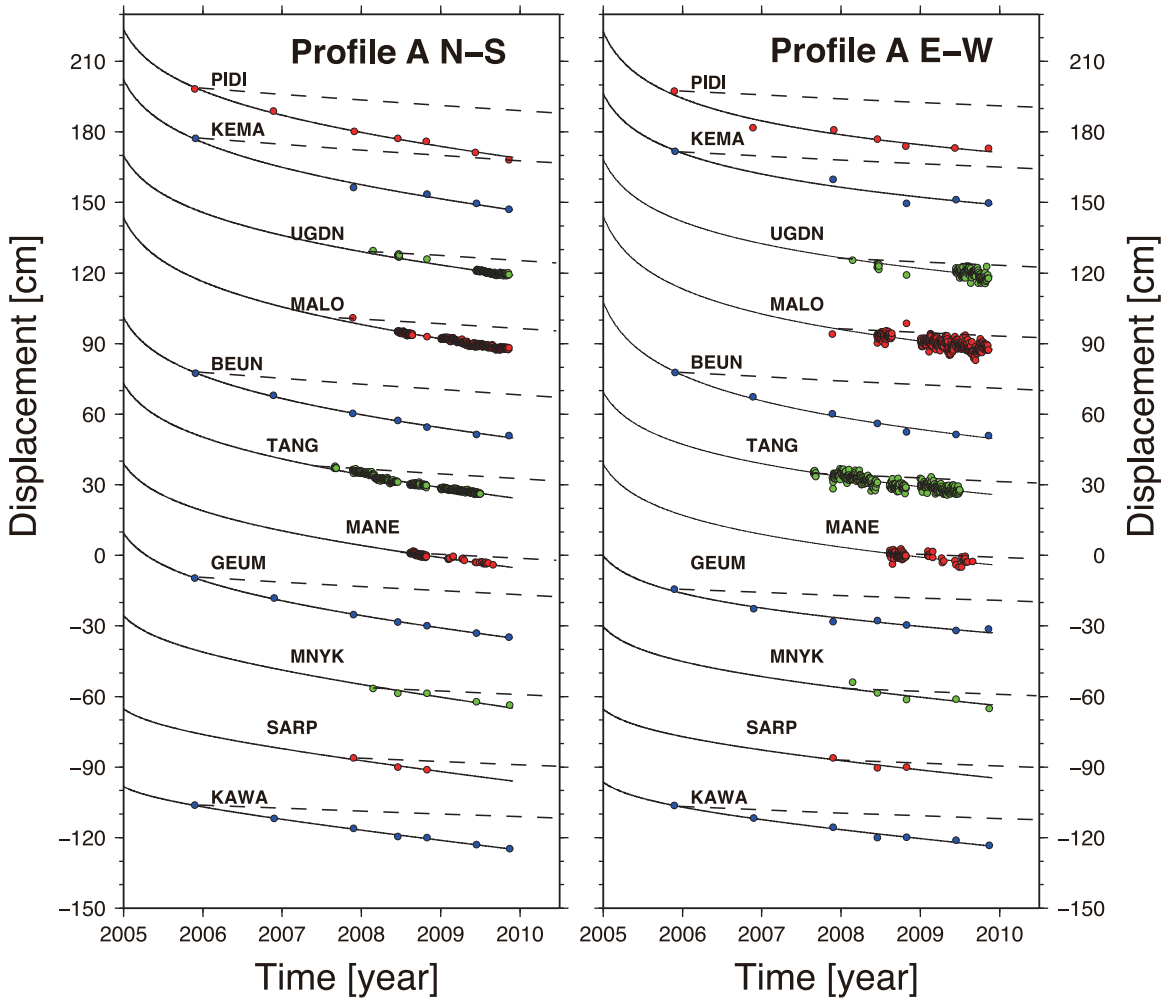

Figure 3. Time series of postseismic displacement at GPS site in PA. Each dashed line is predicted VE response due to the 2004 event. Same description as Figure 2.

southwest were detected [e.g., *Hashimoto et al.*, 2006]. For example, south-westward displacements of 80 cm have been observed at the continuous site, ACEH, in Banda Aceh, over a five year period from February 2005 until November 2009 (see Figure 2).

[9] Postseismic deformation is generally attributed to three classes of phenomena: (1) bulk viscoelastic (VE) relaxation [e.g., *Pollitz et al.*, 2006, 2008], (2) poroelastic (PE) processes [e.g., *Hughes et al.*, 2010], and (3) afterslip on the primary fault in and/or around the region of coseismic slip [e.g., *Hashimoto et al.*, 2006; *Hsu et al.*, 2006]. In case of the 2004 Sumatra-Andaman earthquake, a VE model can fit postseismic deformation for regions exceeding 500 km from source [*Pollitz et al.*, 2006]. However, we find that the VE model does not explain postseismic observations closer to the source. Figures 3 and 4 show predicted time series of crustal deformation due to VE responses as dashed lines. The VE responses are calculated using VISCO1D version 3, which calculates quasi-static deformation on a layered spherical Earth from a specified input fault movement [*Pollitz*, 1997]. In this study, we use a spherically symmetric viscoelastic structure consisting of an elastic plate of thickness 62 km depth underlain by a Burgers body asthenosphere from 62 to 220 km depth and a homogeneous Maxwell viscoelastic upper mantle bellow 220 km depth [*Pollitz et al.*, 2006]. Postseismic deformation due to VE relaxation can be expressed by exponential functions with very long decay times. Thus, time series of VE response has linear trend in our observation period (see Figures 3 and 4). Predicted crustal deformation rate due to VE relaxation in our observation period is about 3 cm/year along lines PA and PB. Spatial variation due to the VE response is smaller than 3 mm/year along lines PA and PB. Thus, we assume the VE effect is linear in time. *Hughes et al.* [2010] suggests that we should expect PE effects of several centimeters in the region of Sumatra. However, PE deformation is expected to decay rapidly (~1 month) in the overriding plate [*Hughes et al.*, 2010]. The PE model does not explain the observed large postseismic deformation. In contrast to the VE and PE models, an afterslip model can fit both near-field and far-field observations [*Hashimoto et al.*, 2006; *Hsu et al.*, 2006]. Thus, in this study, we rely only on an afterslip model to estimate the post-seismic effects associated with the 2004 and 2005 megathrust events.

3.1. Afterslip Model

[10] We show GPS time series in Figures 2, 3, and 4, with the locations of each GPS station shown in Figure 1. The

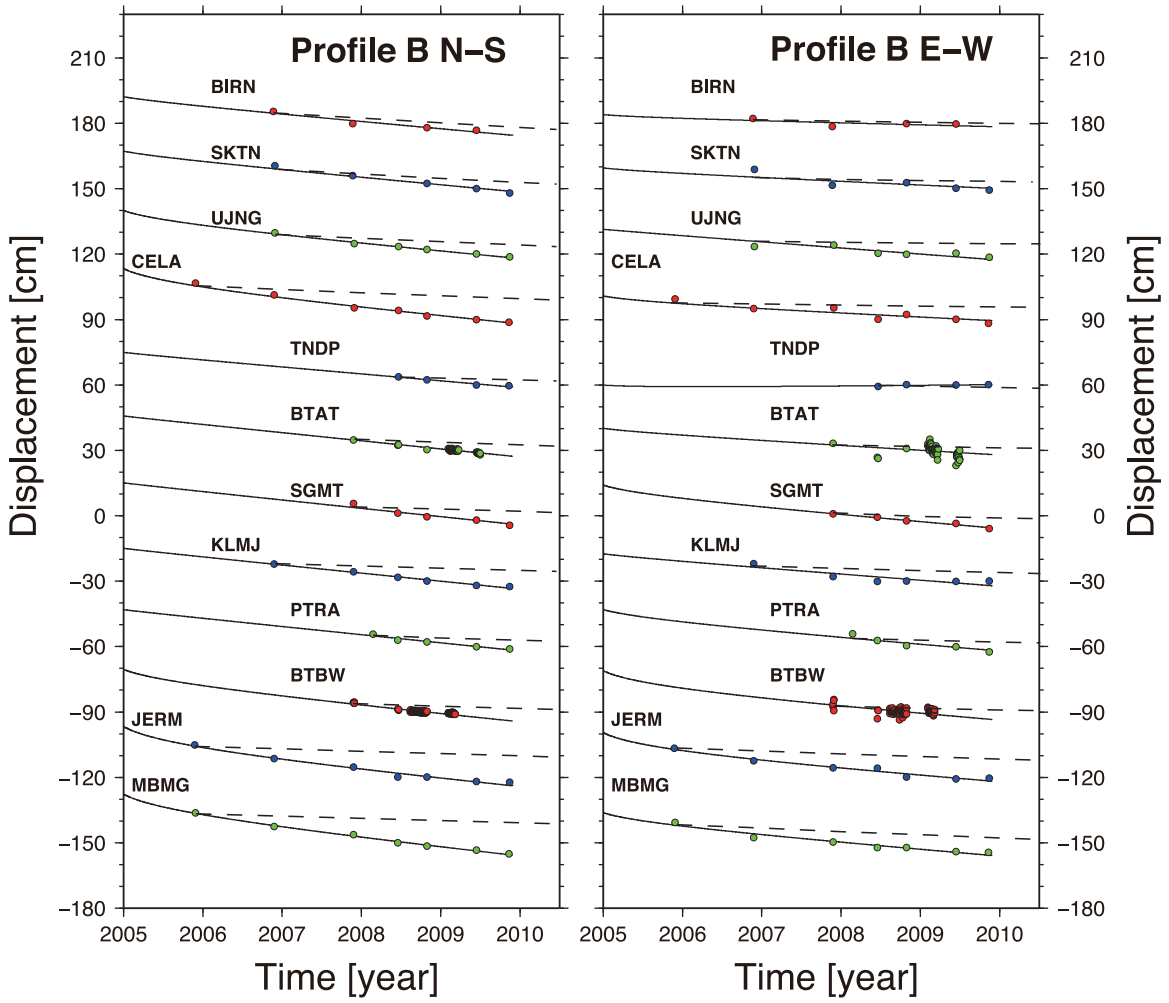

Figure 4. Time series of postseismic displacement at GPS site in PB. Same description as Figure 3.

time series clearly show post-seismic transients associated with the 2004 Sumatra-Andaman and other earthquakes. In the early period of postseismic deformation, we assume that deformation is predominantly driven by frictional afterslip and follows a logarithmic function. Afterslip can be modeled using a rate- and state-dependent friction law. Following *Perfettini and Avouac* [2004], the postseismic displacement resulting from rate-strength brittle creep can be written as

$$U(t) = \alpha V_0 t + \sum_{eq=1}^{3} \left(F_{step}(t - t_{eq}) + \beta_{eq} V_0 t_r \cdot \log\left[1 + d_{eq}\left(\exp\left(\frac{t - t_{eq}}{t_r}\right) - 1\right)\right]\right) \quad (1)$$

where $U(t)$ is the surface displacement, V_0=5 cm/year is the interseismic slip rate on the plate interface, F_{step} is the step function due to the coseismic displacement, α and β_{eq} are geometric factors, t_r is the relaxation time, d_{eq} is the velocity jump due to coseismic stress change, and t is time since December 26, 2004. In this study, we consider the Sumatra-Andaman earthquake (M_w=9.2) on December 26, 2004, the Nias earthquake (M_w=8.7) on March 28, 2005, and the Simeulue earthquake (M_w=7.5) on February 20, 2008. t_{eq} are dates of the modeled earthquakes. In a single-degree-of-freedom system, t_r and d_{eq} in equation (1) can be written as

$$t_r = A\sigma_n/\dot{\tau}$$
$$d_{eq} = \exp\left(\Delta CFS_{eq}/A\sigma_n\right) \quad (2)$$

where A is a rheological parameter, σ_n is the normal stress, $\dot{\tau}$ is the interseismic shear stress rate, and ΔCFS_{eq} is the coseismic coulomb stress change on the creeping patch [*Perfettini and Avouac*, 2004]. In order to determine a rough estimate of rheological parameters, we assume that $A\sigma_n$ and $\dot{\tau}$ are regional parameters, and that t_r and d_{eq} are the same for each component of displacement. Thus, t_r has one value for the region, and d_{eq} is fixed for each earthquake. These assumptions are consistent with previous studies [*Hsu et al.*, 2006]. The values of t_r and d_{eq} are determined by least squares adjustments using ACEH and some sites LEWK, UMLH and BSIM. We obtain t_r equal to about 8.76 years, and values of d_{eq} for the 2004, 2005, and 2008 earthquakes of 46, 1060, and 2650, respectively. These value are consistent with previous studies[e.g., *Hsu et al.*, 2006; *Gahalaut et al.*, 2008]. Figure 2 shows time series of displacement and the associated model fits. The characteristic relaxation time

Table 1. Estimated Parameters From Postseismic Displacement

	Location		North(cm/year)			East(cm/year)		
Site	Latitude	Longitude	V_{int}	αV_0	$\Sigma\beta_{eq}V_0$	V_{int}	αV_0	$\Sigma\beta_{eq}V_0$
ACEH	5.569	95.368	−3.35	−1.48	−1.89	−2.57	−0.52	−2.03
umlh	5.053	95.338	−3.46	−1.20	−2.30	−2.72	−0.68	−2.04
lewk	2.923	95.804	1.91	3.40	−1.47	0.38	1.48	−1.14
bsim	2.409	96.326	0.75	1.92	−1.15	1.20	2.12	−1.00
CALA	4.539	95.718	−3.56	−1.92	−1.64	−2.73	−2.00	−0.73
PIDI	5.366	95.933	−2.98	−1.44	−1.58	−0.71	1.12	−1.85
KEMA	5.234	95.889	−2.96	−1.36	−1.60	−1.09	0.52	−1.59
UGDN	5.223	95.872	−2.95	−1.52	−1.37	−1.28	0.40	−1.68
MALO	5.100	95.894	−2.96	−1.36	−1.60	−1.07	0.92	−2.01
BEUN	5.140	95.883	−2.74	−1.27	−1.47	−1.38	0.53	−1.83
TANG	5.017	95.917	−2.96	−1.64	−1.32	−1.67	−0.32	−1.37
MANE	4.881	96.067	−3.00	−1.84	−1.16	−1.68	−0.36	−1.32
GEUM	4.844	96.125	−3.09	−1.96	−1.19	−1.68	−0.72	−0.96
MNYK	4.628	96.083	−3.96	−2.90	−1.06	−2.44	−1.60	−0.84
SARP	4.519	96.123	−3.75	−2.96	−0.79	−2.84	−2.24	−0.60
KAWA	4.368	96.186	−3.70	−3.06	−0.64	−2.81	−2.28	−0.51
BIRN	5.208	96.822	−3.19	−3.12	−0.09	−0.80	−0.76	−0.12
SKTN	4.986	96.694	−3.26	−3.16	−0.06	−1.58	−1.52	−0.10
UJNG	4.709	96.816	−3.17	−2.88	−0.27	−1.70	−1.56	−0.18
CELA	4.584	96.683	−3.30	−2.96	−0.30	−1.62	−1.48	−0.10
TNDP	4.519	96.628	−3.12	−2.79	−0.02	0.44	0.52	−0.08
BTAT	4.458	96.519	−3.70	−3.62	−0.08	−2.09	−2.04	−0.11
SGMT	4.375	96.513	−3.78	−3.66	−0.12	−2.88	−2.64	−0.24
KLMJ	4.256	96.424	−3.66	−3.64	0.02	−2.73	−2.68	−0.03
PTRA	4.279	96.449	−3.70	−3.68	0.02	−2.83	−2.64	−0.21
BTBW	4.247	96.448	−3.41	−3.00	−0.39	−2.69	−2.32	−0.35
JERM	4.214	96.306	−3.33	−2.92	−0.47	−2.54	−2.16	−0.34
MBMG	4.048	96.247	−3.69	−3.32	−0.43	−2.84	−2.64	−0.28

(t_r=8.76 years) has also been shown to match the decay of aftershocks in the northern part of the Sumatra Island region [*Hsu et al.*, 2006]. Global analyses of aftershocks obtain an average value of t_r of about 10.2 years [*Dieterich*, 1994], similar to our analysis of postseismic deformation in the northern part of the Sumatra island. For comparison, *Parsons* [2002] reports that triggered events globally obey an Omori law with characteristic decay time typically between 7 and 11 years after the main shock. Of course, t_r will depend on local tectonic setting.

[11] When $t < t_r$, equation (1) results in a logarithmic decay of displacement [e.g., *Hsu et al.*, 2006]. While our estimates of t_r is several years, postseismic deformation drops below the accuracy of GPS measurements on shorter timescales. After one year, displacement rates have dropped significantly and are 0.162, 0.009, and 0.004 times that estimated just after the 2004, 2005 and 2008 earthquakes, respectively. The source regions of the 2005 and 2008 earthquakes are located over 100 km from AGNeSS. Although, site TANG, which is located at center of AGNeSS, experienced coseismic displacements of 8 mm southwards and 5 mm eastward due to the 2008 earthquake, postseismic displacement due to this event are below our current measurement capabilities (see Figure 3). Henceforth, we ignore postseismic deformation due to afterslip of the 2005 and 2008 earthquakes.

3.2. Corrected Deformation Rate From Observed Postseismic Deformation

[12] We interpret the velocity at each site as being the sum of the interseismic velocity as well as transient afterslip. Following the 1D model of *Perfettini and Avouac* [2004] there are two terms in equation (1). One is due to ductile flow at depth, which is assumed to be a constant unknown fraction, α, of the velocity, V_0. The second term is the contribution of the creeping brittle fault zone, which is assumed to control postseismic relaxation. The steady state creep rate on the transition zone is a fraction for each earthquake, β_{eq}, of the long-term slip rate, V_0. The interseismic velocity, V_{int}, at GPS site relative to the footwall is described as $(\alpha + \sum \beta_{eq})V_0$ [*Perfettini and Avouac*, 2004; *Hsu et al.*, 2006]. However, the estimated interseismic velocity, V_{int}, will include VE relaxation due to the 2004 event, which we expect to be nearly a constant rate through our observation period. It is difficult to decompose estimated linear velocity into VE relaxation and interseismic velocities. The spatial variation of the predicted VE relaxation velocity in our study area is smaller than 3 mm/year, which is equivalent to our observation error. Figures 3 and 4 show the observed and expected displacement time series at each GPS site. Table 1 shows corrected velocity at each GPS site. However, because of the assumption of a simple 1-D system of springs and sliders, the model provides only a rough estimate of the rheological parameters and does not provide much insight into possible spatial variations of friction parameters. Black arrows in Figure 5 indicate the deformation rate after removing inferred effects due to afterslip. The corrected velocity consists of the linear term, $(\alpha + \Sigma\ \beta_{eq})V_0$, in equation (1). The corrected deformation fields include the effects of elastic coupling on the megathrust and the Sumatran faults as well as any uncertainly in the reference frame, all of which we will consider in the modeling described below. As mentioned above, we assume that the VE response is linear rate in the study area. At the scales of

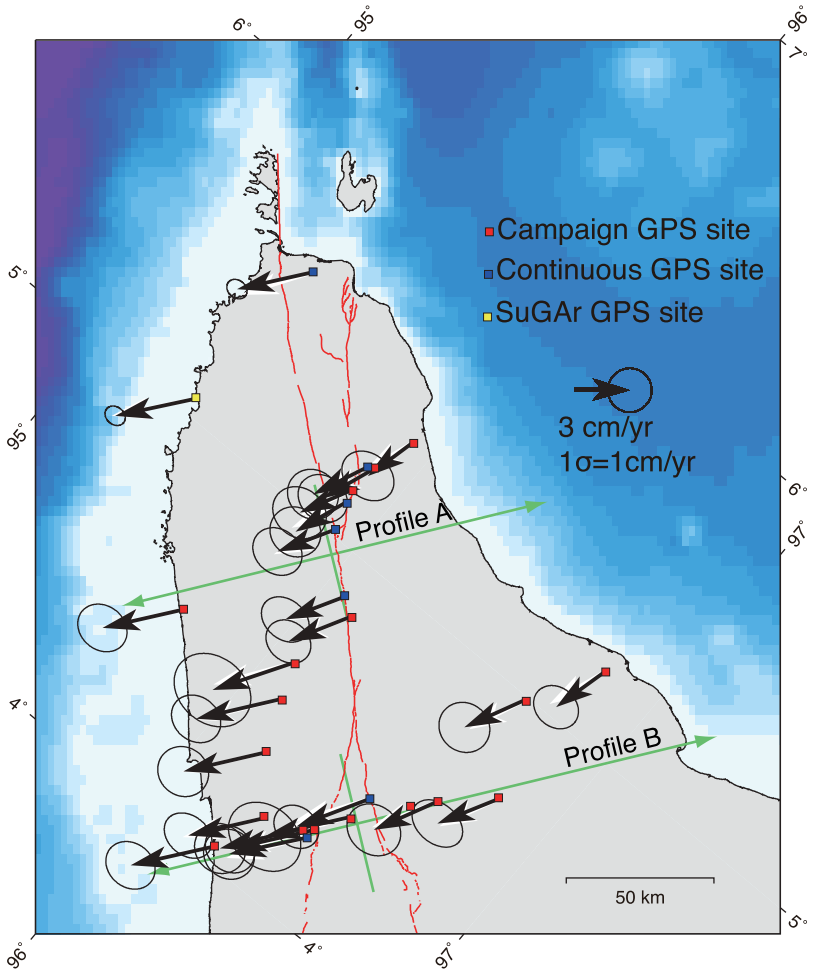

Figure 5. Black arrows mean corrected deformation from postseismic deformation. White arrows are calculated velocity using the no-shallow-creep model. Red, blue, and yellow squares are campaign, continuous, and SuGAr GPS sites, respectively. Green arrows are the fault normal directions. Intersections of green lines are the reference point of surface fault locations for Figures 9, 10, and 11.

this study, the VE response can be lumped into the reference frame uncertainly.

4. Inversion Method

[13] We assume that corrected deformation includes effects of interplate coupling on the subducting plate interface, coupling on the GSF and reference frame motion. We model these effects as

$$\begin{aligned}\mathbf{d} &= \mathbf{G}(\mathbf{m}) \\ &= \mathbf{G}_{SP}\mathbf{m}_{SP} + \mathbf{G}_{GSF}(\mathbf{m}_{GSF}) + \mathbf{G}_{REF}\mathbf{m}_{REF} \end{aligned} \quad (3)$$

where $\mathbf{G}$ and $\mathbf{m}$ are Green's function and model parameters, respectively. $\mathbf{G}_{SP}$ represents the effect of interplate coupling on the curved subducting plate interface and $\mathbf{m}_{SP}$ is the associated backslip vector on the curved subducting plate interface. We introduce a parametric expansion of the fault slip distribution using a finite number of B-splines functions. The estimated interplate coupling ratio is typically less than 0.4. Details of implementation of the plate interface effect are described in Appendix B. The characteristic length scale of crustal deformation due to interplate coupling is longer than 100 km. The typical magnitude of crustal deformation due to coupling of the subducting plate is of order 10^{-7} strain/year. The aperture of AGNeSS is about 100-km-wide normal to trench. Thus, the difference in velocity from one edge to another of AGNeSS is about 1 cm/year. Therefore, in order to remove long wavelength crustal deformation due to a megathrust, we simultaneously estimate the interplate coupling effect.

[14] The second term of equation (3) employs a backslip function for elastic coupling on the GSF system. Assuming pure strike slip motion, $\mathbf{G}_{GSF}(\mathbf{m}_{GSF})$ can be written as

$$\mathbf{G}_{GSF}(\mathbf{m}_{GSF}) = \frac{V_{slip}}{\pi}\left(\tan^{-1}\left(\frac{X_{GPS}+X_{shift}}{Z_{lock}}\right) + \tan^{-1}\left(\frac{Z_{creep}}{X_{GPS}+X_{shift}}\right)\right) \quad (4)$$

where V_{slip}, Z_{lock} and Z_{creep} are the slip deficit rate, locking depth and creeping depth on the GSF, respectively [*Chinnery*, 1961; *Segall*, 2010]. Thus, the GSF is locked

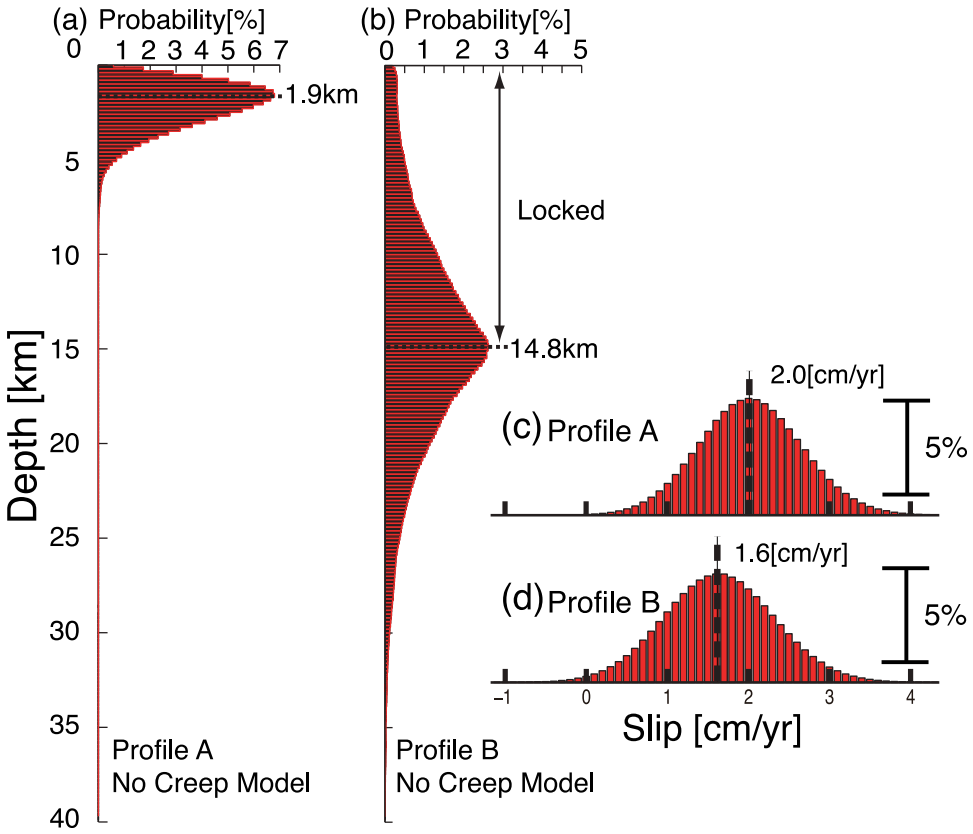

Figure 6. Marginal posterior PDF of locking depths, Z_{lock}, and slip deficit rates, V_{slip}, for each profile region in the no-shallow-creep model. (a, b) The marginal posterior PDF of locking under limit depths in the each region. (c, d) Marginal posterior PDF of slip deficit rate in the each profile. Positive value is right lateral slip. Dotted lines of all figures mean maximum likelihood estimation value.

from Z_{creep} to Z_{lock}. This term includes an apparent block motion, across the GSF. To account for mislocation of the fault trace, we introduce X_{GPS} and X_{shift} in equation (4), representing the perpendicular distance between the surface trace of the GSF and each GPS site and differences distance between X_{GPS} and actual locking fault trace, respectively. Thus, X_{GPS} is a known constant value for each GPS site, and X_{shift} is an unknown parameter for each observation profile. We estimate V_{slip}, Z_{lock}, Z_{creep}, and X_{shift}, for each profile. The third term of equation (3) allows us to correct the reference flame for the entire GPS network.

[15] We estimate all the unknown parameters in equation (3) using a fully Bayesian approach [e.g., *Tarantola*, 2005]. In a Bayesian formulation, prior information on a vector of unknowns, **m**, is expressed by a prior probability density function (PDF), $p(\mathbf{m})$. The posterior PDF, $p(\mathbf{m}|\mathbf{d})$ denotes the probability density of unknowns, **m**, given, **d**. Specifically, Bayes' theorem is

$$p(\mathbf{m}|\mathbf{d}) = \frac{p(\mathbf{d}|\mathbf{m})p(\mathbf{m})}{\int_{-\infty}^{+\infty} p(\mathbf{d}|\mathbf{m})p(\mathbf{m})d\mathbf{m}} \tag{5}$$

where $p(\mathbf{d}|\mathbf{m})$ is the PDF of **d** given **m**, and $\int_{-\infty}^{+\infty} p(\mathbf{d}|\mathbf{m})p(\mathbf{m})d\mathbf{m}$ normalizes the posterior PDF, which is independent of **m**. Therefore,we can restate equation (5) as

$$p(\mathbf{m}|\mathbf{d}) \propto p(\mathbf{d}|\mathbf{m})p(\mathbf{m}). \tag{6}$$

[16] We assume that the PDF, $p(\mathbf{d}|\mathbf{m})$, follows a Gaussian distribution of mean, $\mathbf{G}(\mathbf{m})$, and covariance matrix, σ_d, such that

$$p(\mathbf{d}|\mathbf{m}) = (2\pi)^{-\frac{N}{2}}|\sigma_d|^{-\frac{1}{2}}\exp\left[-\frac{1}{2}(\mathbf{d}-\mathbf{G}(\mathbf{m}))^T\sigma_d^{-1}(\mathbf{d}-\mathbf{G}(\mathbf{m}))\right] \tag{7}$$

where N is number of observation. Given a prior PDF, $p(\mathbf{m})$, the posterior PDF, $p(\mathbf{m}|\mathbf{d})$, is estimated using equation (6).

[17] We assume a homogeneous prior PDF, $p(\mathbf{m})$, which in this case is a uniform value. We make two modifications to the prior, first is the physically sensible constraint on the locking and creeping depths such that m_{lock} is deeper than m_{creep}. We also assume that the magnitude of interplate coupling velocity is less than 5 cm/year, corresponding to the velocity of the subducting India/Australia plate relative to the Sunda plate, which is about 47 mm/year in this region [e.g., *Socquet et al.*, 2006; *Delescluse and Chamotrooke*, 2007].

[18] The posterior PDF, $p(\mathbf{m}|\mathbf{d})$, is a non-Gaussian distribution. Because closed-form analytical expressions are not available, we construct a discrete representation of the posterior PDF by sampling with a Markov Chain Monte Carlo (MCMC) method. Specifically, we employ a Metropolis-Hastings (M-H) algorithm. For a detailed explanation of MCMC method and M-H algorithm, we refer the reader to other texts on the topic [e.g., *Metropolis et al.*, 1953;

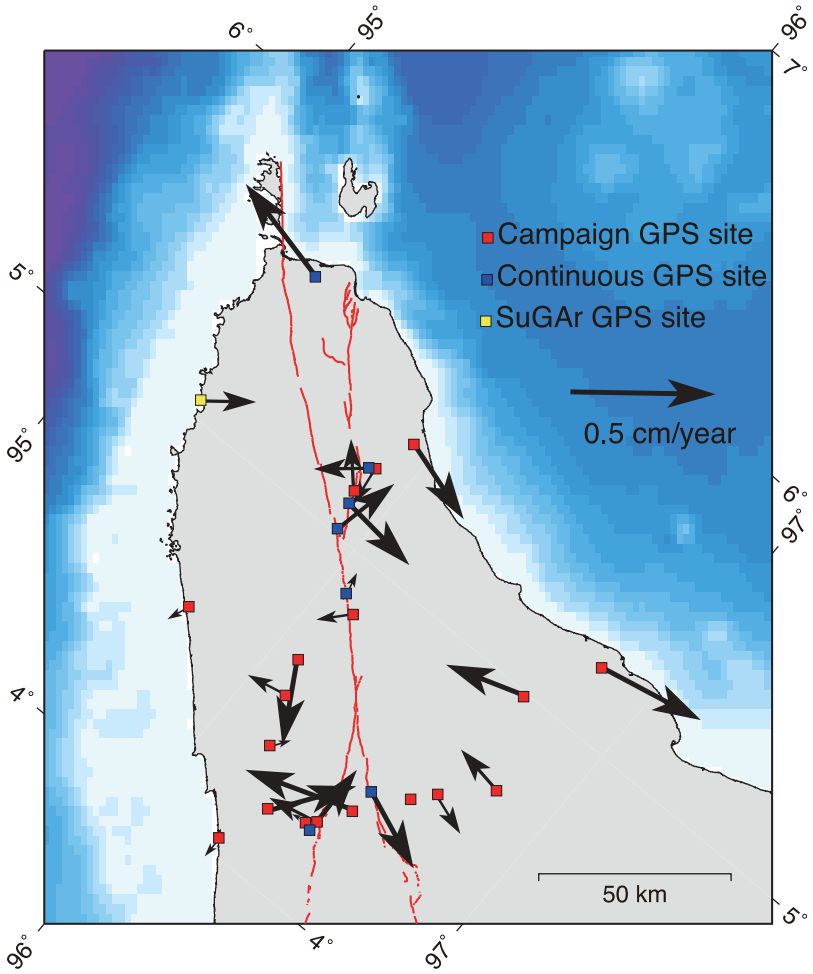

Figure 7. Spatial distribution of the residual velocities using the no-shallow-creep model.

Hastings, 1970; *Gamerman*, 1997]. In the M-H algorithm, we discard the first 1.0×10^8 samples as having memory of the initial parameters and regard the subsequent 3.0×10^8 samples as samples drawn from the posterior PDF. Note that we do not introduce any smoothing or damping.

5. Results and Discussion

[19] We investigate two classes of models of elastic coupling on the GSF. One is a no-shallow-creep model, which assumes locking between surface and locking depth, Z_{lock}, and the another class allows for shallow creep. Figure 6 shows the posterior PDF for the no-shallow-creep model. The estimated locking depth, Z_{lock}, for PA and PB are 1.9 ± 1.2 km and 14.8 ± 3.4 km depth, respectively. We suspect that creep occurs on the segment of the GSF sampled by PA. We discuss this creep later. The estimated slip deficit rates, V_{slip}, of for PA and PB are 2.0 ± 0.6 and 1.6 ± 0.6 cm/year, respectively. Estimated slip deficit rates are smaller than inferred from geological studies [e.g., *Bennett et al.*, 1981; *Sieh and Natawidjaja*, 2000]. For example, *Bennett et al.* [1981] suggests that long-term slip rate in this region is 3.8 ± 0.4 cm/year from geological studies. Our results are not consistent with previous geological studies. A discrepancy between geodetic and geologic rates may be reconcilable if fault behavior is non-stationary whereby a given fault experiences clustered earthquakes with a number of large earthquakes on the same fault occurring in a short period of time followed by an extended quiescent period. In the later stages between a cluster or even within the period between two individual earthquakes, the apparent geodetic slip rate may appear to be substantially slower than the long-term average [i.e., *Savage and Prescott*, 1978; *Meade and Hager*, 2005; *DiCaprio et al.*, 2008]. On the other hand, the estimated slip deficit rate from a previous geodetic study is 0.5 ± 0.2 cm/year, based on earlier GPS data in the Banda Aceh transect about 50 km northwest of our study area [*Genrich et al.*, 2000]. We also show predicted deformation and spatial residual in Figures 5 and 7. These residuals would be spatially random if they were mainly due to GPS observation error.

[20] Fault length, L, and width, W, are empirically found to be approximately related in strike slip earthquakes with the length of the slipping area being approximately twice the down dip extent [*Geller*, 1976]. In the case of PB, if the fault width is equal to the estimated locking depth (14.8 km), we can infer an estimated rupture length of about 29.6 ± 6.8 km, corresponded to a magnitude 7 class earthquake.

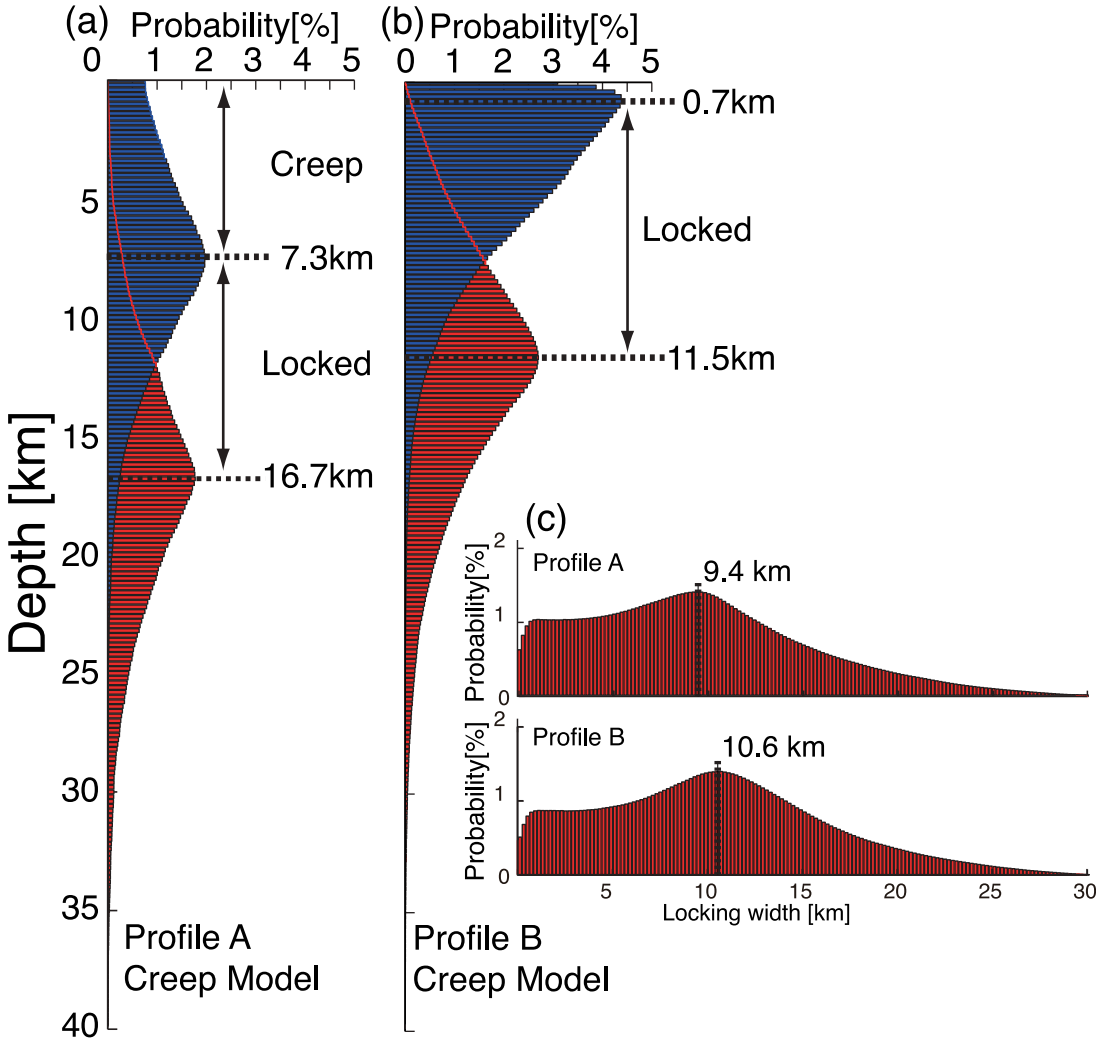

Figure 8. Marginal posterior PDF of locking depth, Z_{lock}, creeping depths, Z_{creep}, and slip deficit rates, V_{slip}, in the shallow-creep model. (a, b) Marginal posterior PDF of the upper (blue) and lower (red) limits of the locked portion for each profile. (c) Marginal posterior PDF of the width of the locked zone. Dashed lines of all figure indicates the maximum likelihood value.

Such events are not rare on the GSF system (see Figure 1), for example, a M_w 7.8 earthquake occurred in 1892.

[21] In order to evaluate seismic potential, the integral of the product slip deficit rate (1.6 cm/year) times the estimated locking depth is about 236.8 ± 122 m^2/year, which is equivalent to an accumulation rate of seismic moment of about 7.1 ± 3.7 × 10^{12} N·m/year per meter of fault length, using a rigidity for the crust of 30 GPa. The accumulated seismic moment on a 30-km-long segment since the last earthquake, which probably occurred about 170 years ago [*Bellier et al.*, 1997; *Sieh and Natawidjaja*, 2000], is M_o=3.6 ± 1.9 × 10^{19} N·m. Thus, the GSF on the region of PB appears capable of producing earthquake of magnitude 7.

5.1. Estimated Creep Fault

[22] In the region of PA, the no-shallow-creep model finds a slip deficit rate and locking depth of 2.0 ± 0.6 cm/year and 1.9 ± 1.2 km, respectively. In effect, the shallow locking depth of PA implies that entire fault is creeping, and that only small earthquakes are likely.

[23] On the other hand, we can explore a model that allows for shallow creep. Figure 8 shows posterior PDF of the locking and creeping depths for each profile. Estimated shallow creep depths for PA and PB are 7.3 ± 4.8 and 0.7 ± 1.8 km depth, respectively. We show the fault-parallel component of velocity profile across the GSF as predicted by the two models (see Figure 9). Discriminating between the creep and no-creep models is not possible with the current geodetic network. We also find no significant fault normal component deformation (see Figure 10). For comparison, Figure 11 shows the fault-parallel component of uncorrected velocity profile across the GSF. The deformations are similar to corrected deformation (see Figure 9). Because, the characteristic length scale of crustal deformation due to afterslip is longer than 100 km. The GSF-parallel direction is normal to direction of dominant postseismic deformation. Both the afterslip component and the linear viscous/reference frame component are small influence on the GSF-parallel direction component.

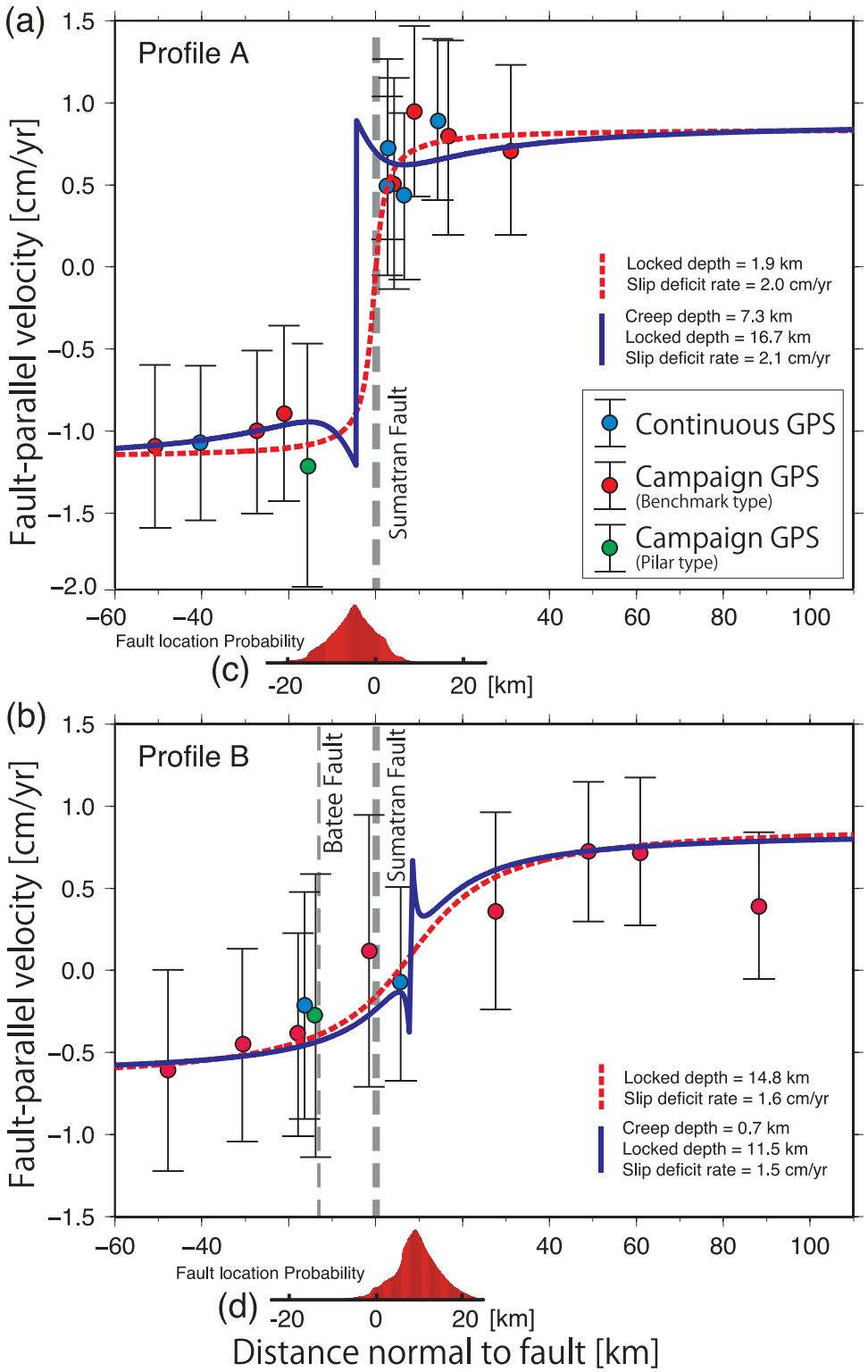

Figure 9. Fault-parallel component of corrected velocity across the GSF. Positive values of fault-parallel velocity in the south-eastern direction. (a) PA and (b) PB. Blue, red, and green circles denote continuous, campaign observation with benchmark type, and campaign observation with pillar type, respectively. Error bars are one standard deviation. The Sumatran fault is approximately located at x = 0. (c, d) Marginal posterior PDFs of fault locations, X_{shift}, at PA and PB, respectively. The fault location PDFs are based on the shallow-creep model.

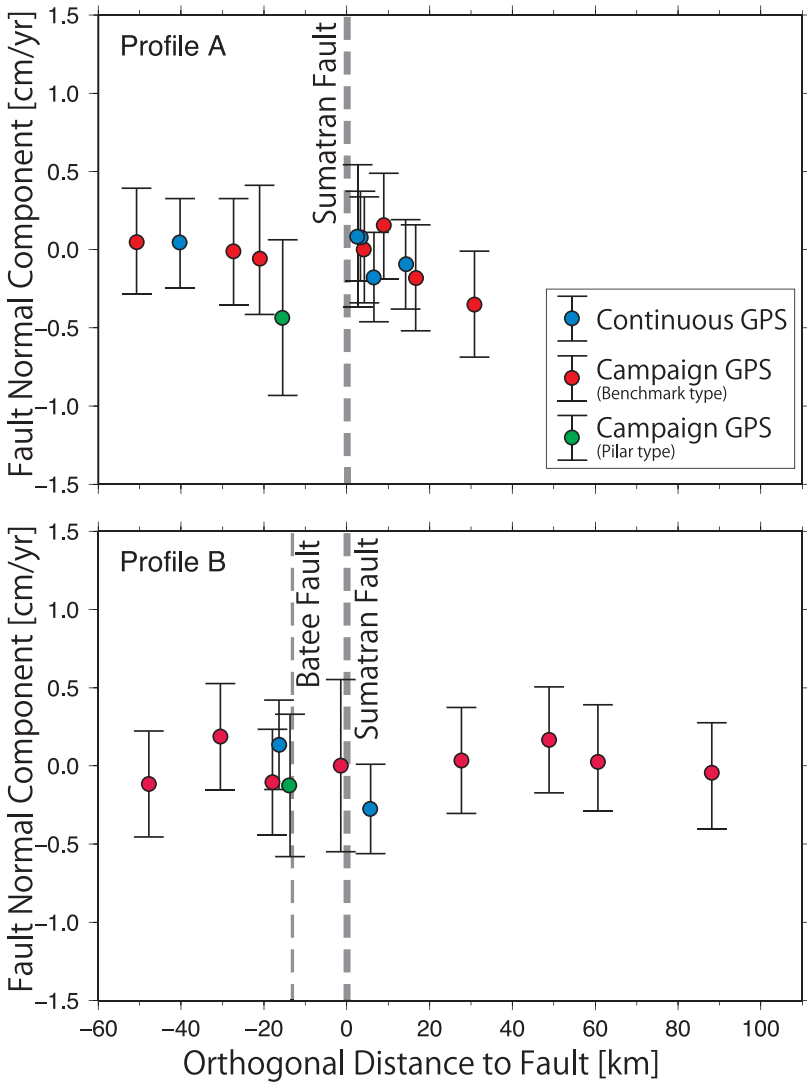

Figure 10. Fault-normal component of corrected velocity profile across the GSF. The positive value of fault-normal velocity is the south-western direction. Other descriptions are same as Figure 9.

[24] The fault in the region of PB probably does not experience shallow creep. Although, the distance between PA and PB is only 50 km, the GSF appears to experience spatially heterogeneous coupling. Indeed, this segment of the fault is geologically quite complex [e.g., *Bellier and Sebrier*, 1995; *Sieh and Natawidjaja*, 2000]. Especially, there is large intrusive rock at center of PA [*Bennett et al.*, 1981].

[25] Figure 8c shows the posterior PDF of the width of fault locking. The estimated width of the locked zone for the region of PA and PB are 9.4 ± 6.4 and 10.6 ± 7.2 km, respectively. Thus, despite the possibility of shallow creep in the upper 7 km depth, the fault segment near PA appears capable of producing significant earthquakes.

[26] Finally, the Batee fault is a major right-lateral strike-slip fault that diverges from the GSF (see Figure 7 and 9). *Sieh and Natawidjaja* [2000] suggests the Batee fault does not appear to be active. The lack of clear small offsets suggests either no activity in the past few tens of thousands of years or activity at a rate much lower than along the GSF. However, *Bellier and Sebrier* [1995] estimate 1.2 ± 0.5 cm/year as long-term offset rate from geomorphic evidence. Our result does not require any significant slip deficit rate on the Batee fault (see Figure 9).

6. Conclusion

[27] Beginning in 2005, we established AGNeSS in the northwestern part of the Sumatra Island. AGNeSS consist of 7 continuous and 17 campaign GPS sites spanning the northwestern segment of the GSF system. AGNeSS observes postseismic deformation exceeding 80 cm in five years following the 2004 Sumatra-Andaman earthquake. We remove postseismic deformation due to afterslip from observed postseismic deformation using a parameterized afterslip model. The afterslip model fits the observed postseismic deformation well. The characteristic relaxation time, t_r, is 8.76 years from time series of postseismic deformation.

[28] We evaluate a seismic potential on the northwestern part of the GSF using the corrected deformation field. The GSF near PA may be creeping in the upper 7.3 ± 4.8 km

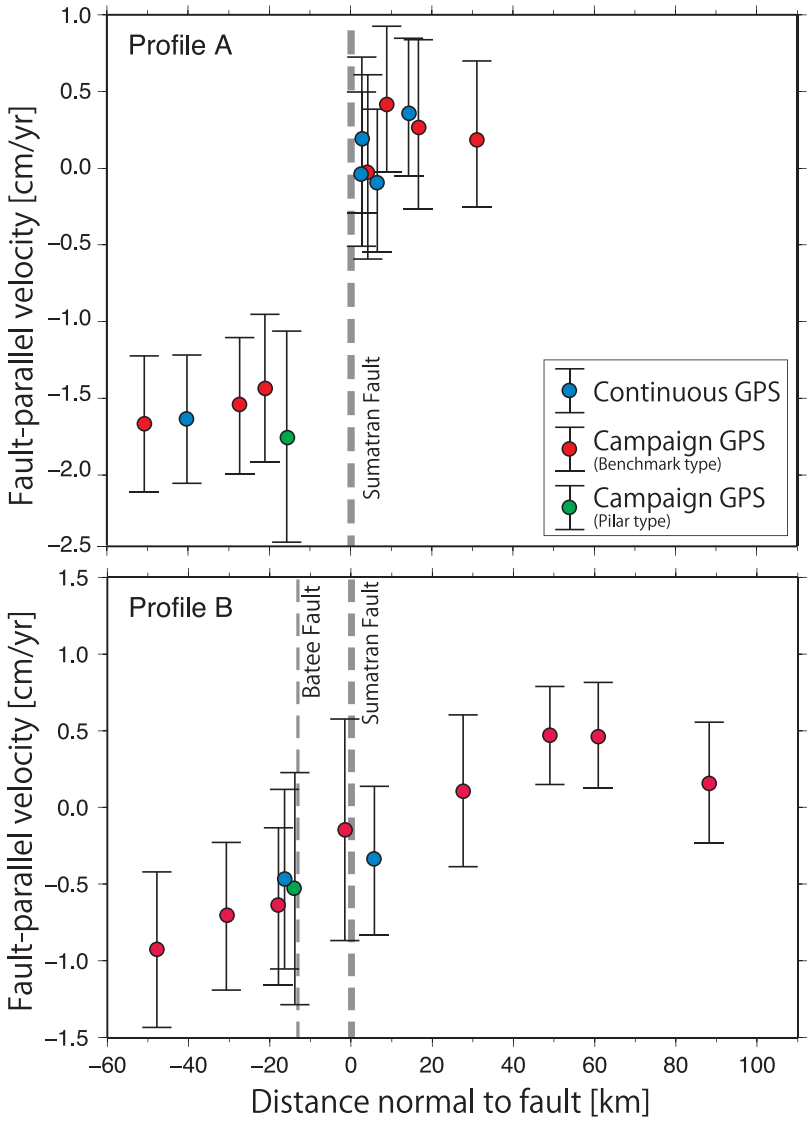

Figure 11. Fault-parallel component of uncorrected velocity across the GSF. Using period is from 2008 to 2009. Other descriptions are same as Figure 9.

with an estimated slip deficit rate of 2.0 ± 0.6 cm/year. Despite the shallow creep, the estimated width of the locked zone is 9.4 ± 6.4 km. Thus, this fault segment appears to be capable of producing significant earthquakes. Further to the south near PB, the estimated locking depth and slip deficit rate are 14.8 ± 3.4 km depth and 1.6 ± 0.6 cm/year, respectively. This result suggests that the accumulated seismic moment in 170 years corresponds to an earthquake of magnitude 7.

Appendix A: Monumentation and Data Reduction

[29] All GPS sites are either located on hard rock or on a deeply buried cement pillar reinforced with iron rods with proper benchmarks. For continuous GPS sites, an approximately 1.5-m-high concrete pillar supports the GPS antenna as well as the GPS receiver, download device, solar controller, and backup battery are stored in a steel box embedded in the foundation. Due to the risk of theft, we use older Trimble 4000SSI receivers set to sample every second. The data are automatically downloaded and converted to 30-sec samples. 1-sec data are stored on site using a three month ring buffer. For campaign GPS sites, we use two styles of monuments, one using a 1.5-m-high steel pipe pillar imbedded in a 1.0 m deep foundation, with the antennae directly attached to the pipe. The another monument type simply uses a 1.5 m deep foundation with a embedded benchmark. We measure the benchmarks using a tripod installation. For all campaign GPS measurement, we used Trimble 5700 receivers and occupied each site for between 24 and 48 hours.

[30] To estimate the daily positions, we used the Bernese software version 5.0. We include the permanent IGS sites (KUNM, PIMO, HYDE, and COCO), the IGS final ephemeris, earth rotation parameters, ionosphere model parameters, and differential code biases for satellites and receiver. We use the coefficients of ocean tidal loading model based on FES2004 [*Lyard et al.*, 2006] from the Onsala Space

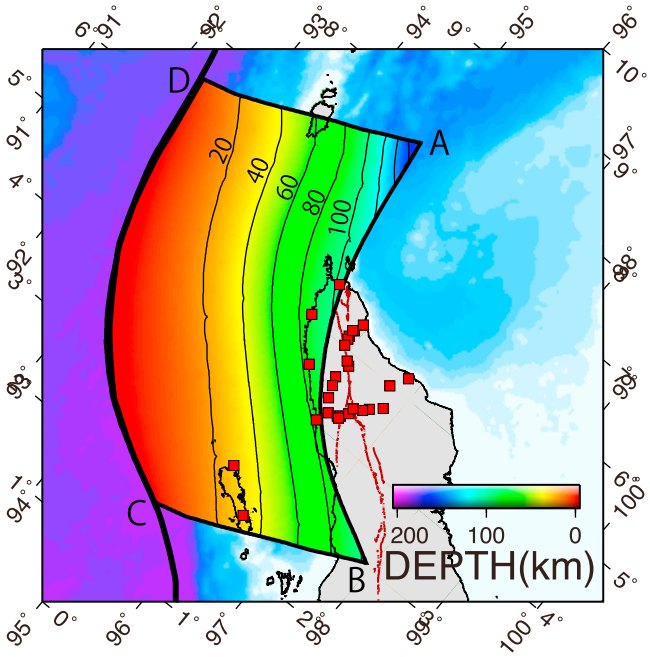

Figure B1. Model outline of the curved plate interface on the Sunda subduction zone. The modeled plate interface is 700 km × 500 km. Red squares are GPS sites used. Letters at the corners of the model area indicate the positions on the map of the equivalent points shown in Figure 13.

Observatory [*Penna et al.*, 2007]. The GPS velocities, displacements and their uncertainties are calculated with respect to ITRF2005 [*Altamimi et al.*, 2007]. Typical errors of the daily positions in the north, east, and vertical components are 0.43, 0.62 and 0.81 cm, respectively. For campaign sites, there is an additional error due to resetting of the tripod. Typical resetting error is less than 0.2 cm.

Appendix B: Implementation of Estimating Plate Interface Effect

[31] In order to infer the spatial interplate coupling distribution, we introduce a curved plate interface geometry based on the Slab Models for Subduction Zones [*Hayes et al.*, 2009; *Hayes and Wald*, 2009]. To estimate coefficients of interplate coupling on the curved plate interface, we introduce a parametric expansion of the fault slip distribution using a finite number of known basis functions. We represent the spatial distribution of each slip component, Δu_j, by linear combination of a finite number (k and l) of basis function, Φ_{kl}, defined on the plane, ξ, as

$$\Delta u_j(\xi_1, \xi_2) = \sum_{k=1}^{K} \sum_{l=1}^{L} a_{jkl} \Phi_{kl}(\xi_1, \xi_2) \tag{B1}$$

where a is coefficient of B-spline function, $\Phi_{kl}(\xi_1, \xi_2)$. Let d_i be the observed displacement at surface, $G_{ij}(\xi)$ is the derivative of Green's tensor with respect to ξ. Surface displacement, d_i, describe to figure out the integration with respect to ξ, and the convolution with Green's function and

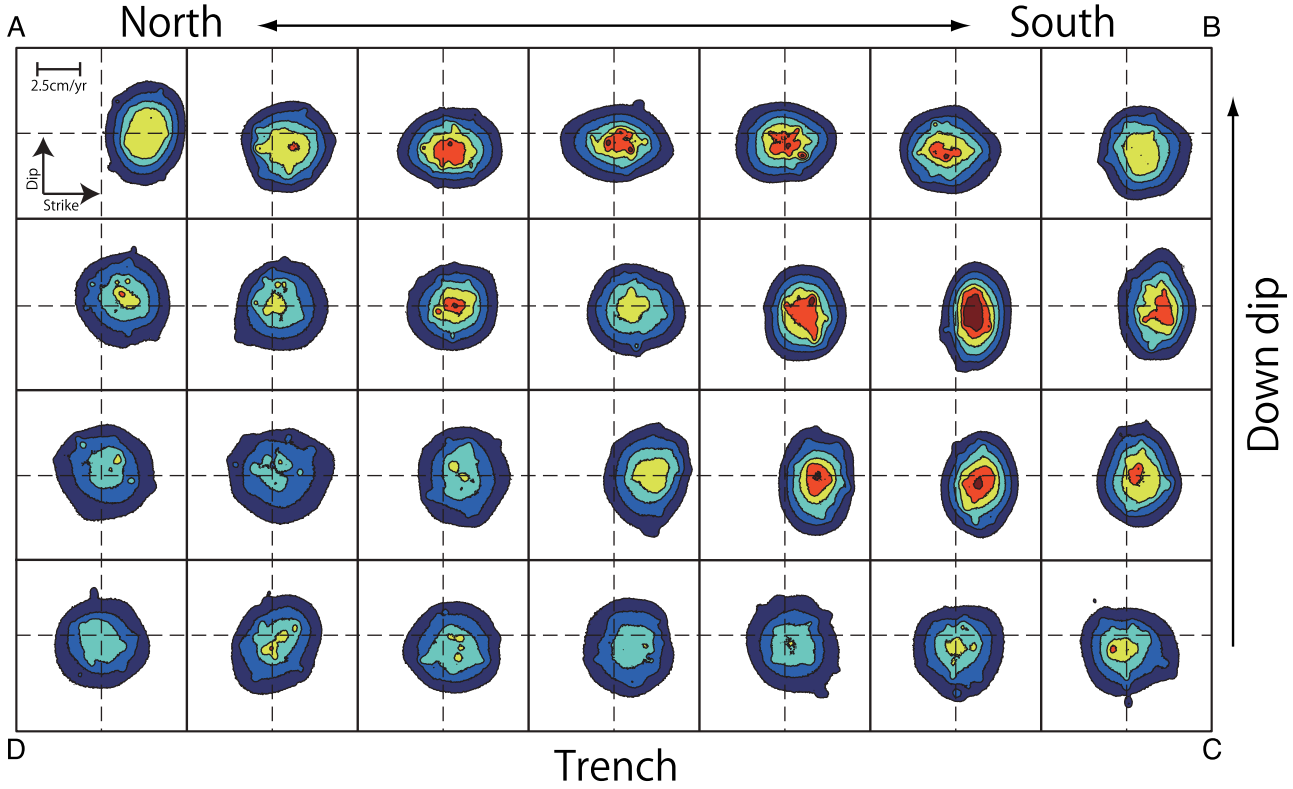

Figure B2. Marginal posterior PDF of slip deficit on the plate interface. Each subsection corresponds to each sub fault, respectively. Each posterior PDF of each subsection denote slip vector. Interval of each contour is 0.5 %. Letters correspond to locations shown in Figure 12.

fault slip. Then, using (equation B1), we may write observation equations as

$$d_i = \sum_{j=1}^{2} \int_{\xi} G_{ij}(\xi_1, \xi_2) \Delta u_j(\xi_1, \xi_2) d\xi = \sum_{j=1}^{2} \sum_{k=1}^{K} \sum_{l=1}^{L} a_{jkl} \int_{\xi} G_{ij}(\xi_1, \xi_2) \Phi_{kl}(\xi_1, \xi_2) d\xi = \sum_{j=1}^{2} \sum_{k=1}^{K} \sum_{l=1}^{L} H_{ijkl} a_{jkl} \quad \text{(B2)}$$

Substituting this expression into equation (3), then we can evaluate the posterior PDF straightforwardly. For more detail of implimention of the B-spline formulations, please see *Yabuki and Matsu'ura* [1992].

[32] We set a curved plate interface on the Sunda subduction zone (see Figure B1). We distribute 10×7 bicubic B-splines so that they cover homogeneously the whole model fault region. The distribution of each slip component on the rectangular fault plane is represented by the superposition of the 10×7 bicubic B-splines with various amplitudes. We divide the rectangular model fault into 7×4 subsections. Figure B2 shows the posterior PDF distribution at each subsection. The posterior PDF on the offshore region is low and wider than near land. Estimated interplate coupling ratio is typically less than 0.4. The velocity of subducting plate India/Australia relative to Sunda is about 47 mm/year in this region [e.g., *Socquet et al.*, 2006; *Delescluse and Chamotrooke*, 2007]. Although our method dose not introduce smoothing hyper-parameters, the estimated coupling ratio are reasonable value. Because, a purpose of this implication in interplate coupling estimation is to remove long wavelength crustal deformation due to the plate interface effect, we do not discuss a pattern and amplitude of interplate coupling distribution.

[33] **Acknowledgments.** We thank the Editor, Tom Parsons, and two reviewers, Danny Hilman Natawidjaja and an anonymous reviewer, for their thoughtful reviews and valuable comments that helped to improve the manuscript. This is Caltech Seismological Laboratory contribution number 10076 and Caltech Tectonics Observatory contribution number 197. This material is supported by the grants-in-aid for scientific research (19253003 and 23740337) of MEXT of Japan.

References

Altamimi, Z., X. Collilieux, J. Legrand, B. Garayt, and C. Boucher (2007), ITRF2005: A new release of the international terrestrial reference frame based on time series of station positions and earth orientation parameters, *J. Geophys. Res.*, *112*, B09401, doi:10.1029/2007JB004949.

Bellier, O., and M. Sebrier (1995), Is the slip rate variation on the Great Sumatran Fault accommodated by fore-arc stretching, *Geophys. Res. Lett.*, *22*, 1969–1972.

Bellier, O., M. Sebrier, S. Pramumijoyo, T. Beaudouin, H. Harjono, I. Bahar, and O. Forni (1997), Paleoseismicity and seismic hazard along the Great Sumatran Fault (Indonesia), *J. Geodyn.*, *24*, 169–183.

Bennett, J. D., et al. (1981), Geologic map of Banda Aceh Quadrangle, North Sumatra, 1:250000, Geol. Res. and Dev. Cent., Bandung, Indonesia.

Chinnery, M. A. (1961), The deformation of the ground around surface faults, *Bull. Seismol. Soc. Am.*, *51*, 255–372.

Delescluse, M., and N. Chamotrooke (2007), Instantaneous deformation and kinematics of the India-Australia plate, *Geophys. J. Int.*, *168*, 818–842.

DiCaprio, C. J., M. Simons, S. J. Kenner, and C. A. Williams (2008), Post-seismic reloading and temporal clustering on a single fault, *Geophys. J. Int.*, *172*, 581–592.

Dieterich, J. (1994), A constitutive law for rate of earthquake production and its application to earthquake clustering, *J. Geophys. Res.*, *99*, 2601–2618.

Gahalaut, V. K., et al. (2008), GPS measurements of postseismic deformation in the Andaman Nicobar region following the Giant 2004 Sumatra-Andaman earthquake, *J. Geophys. Res.*, *113*, B08401, doi:10.1029/2007JB005511.

Gamerman, D. (1997), Sampling from the posterior distribution in generalized linear mixed models, *Stat. Comput.*, *7*, 57–68.

Geller, R. J. (1976), Scaling relations for earthquake source parameters and magnitudes, *Bull. Seismol. Soc. Am.*, *66*, 1501–1523.

Genrich, J. F., Y. Bock, R. McCaffrey, L. Prawirodirdjo, C. W. Stevens, S. S. O. Puntodewo, C. Subarya, and S. Wdowinski (2000), Distribution of slip at the northern Sumatran Fault System, *J. Geophys. Res.*, *105*, 28,327–28,341.

Hashimoto, M., N. Choosakul, M. Hashizume, S. Takemoto, H. Takiguchi, Y. Fukuda, and K. Fujimori (2006), Crustal deformations associated with the Great Sumatra-Andaman earthquake deduced from continuous GPS observation, *Earth Planets Space*, *58*, 127–139.

Hastings, W. K. (1970), Monte-Carlo sampling methods using Markov chains and their applications, *Biometrika*, *57*, 97–109.

Hayes, G. P., and D. J. Wald (2009), Developing framework to constrain the geometry of the seismic rupture plane on subduction interfaces a priori: A probabilistic approach, *Geophys. J. Int.*, *176*, 951–964.

Hayes, G. P., D. J. Wald, and K. Keranen (2009), Advancing techniques to constrain the geometry of the seismic rupture plane on subduction interfaces a priori: Higher-order functional fits, *Geochem. Geophys. Geosyst.*, *10*, Q09006, doi:10.1029/2009GC002633.

Hsu, Y. J., M. Simons, J. P. Avouac, J. Galetzka, K. Sieh, M. Chlieh, D. Natawidjaja, L. Prawirodirdjo, and Y. Bock (2006), Frictional afterslip following the 2005 Nias-Simeulue earthquake, Sumatra, *Science*, *312*, 1921–1926.

Hughes, K. L., T. Masterlark, and W. D. Mooney (2010), Poroelastic stress-triggering of the 2005 M8.7 Nias earthquake by the 2004 M9.2 Sumatra Andaman earthquake, *Earth Planet. Sci. Lett.*, *293*, 289–299, doi:10.1016/j.epsl.2010.02.043.

Lyard, F., F. Lefevre, T. Letellier, and O. Francis (2006), Modelling the global ocean tides: Modern insights from FES2004, *Ocean Dyn.*, *56*, 394–415.

Meade, B. J., and B. H. Hager (2005), Block models of crustal motion in southern California constrained by GPS measurements, *J. Geophys. Res.*, *110*, B03403, doi:10.1029/2004JB003209.

Metropolis, N., A. W. Rosenbluth, M. N. Rosenbluth, A. H. Teller, and E. Teller (1953), Equation of state calculations by fast computing machines, *J. Chem. Phys.*, *21*, 1087–1092.

Natawidjaja, D., and K. Sieh (1994), Slip rates along the sumatran trans current fault and its tectonics significance, paper presented at Conference on Tectonic Evolution of Southeast Asia, Geol. Soc., London.

Parsons, T. (2002), Global Omori law decay of triggered earthquakes: Large aftershocks outside the classical aftershock zone, *J. Geophys. Res.*, *107*(B9), 2199, doi:10.1029/2001JB000646.

Penna, N. T., M. A. King, and M. P. Stewart (2007), GPS height time series: Short-period origins of spurious long-period signals, *J. Geophys. Res.*, *112*, B02402, doi:10.1029/2005JB004047.

Perfettini, H., and J. P. Avouac (2004), Postseismic relaxation driven by brittle creep: A possible mechanism to reconcile geodetic measurements and the decay rate of aftershocks, application to the Chi-Chi earthquake, Taiwan, *J. Geophys. Res.*, *109*, B02304, doi:10.1029/2003JB002488.

Pollitz, F. F. (1997), Gravitational viscoelastic postseismic relaxation on a layered spherical Earth, *J. Geophys. Res.*, *102*, 17,921–17,941.

Pollitz, F. F., R. Burgmann, and P. Banerjee (2006), Post-seismic relaxation following the Great 2004 Sumatra-Andaman earthquake on a compressible self-gravitating Earth, *Geophys. J. Int.*, *167*, 397–420.

Pollitz, F. F., P. Banerjee, K. Grijalva, B. Nagarajan, and R. Burgmann (2008), Effect of 3-D viscoelastic structure on post-seismic relaxation from the 2004 M = 9.2 Sumatra earthquake, *Geophys. J. Int.*, *173*, 189–204.

Savage, J. C., and W. H. Prescott (1978), Asthenosphere readjustment and earthquake cycle, *J. Geophys. Res.*, *83*(B7), 3369–3376.

Segall, P. (2010), *Earthquake and Volcano Deformation*, Princeton Univ. Press, N. J.

Sieh, K., and D. Natawidjaja (2000), Neotectonics of the Sumatran Fault, Indonesia, *J. Geophys. Res.*, *105*, 28,295–28,326.

Sieh, K. and J. Zachariasen, Y. Bock, L. Edwards, F. Taylor, and P. Gans (1994), Active tectonics of Sumatra, *Geol. Soc. Am. Abstr. Programs*, *26*, 382.

Socquet, A., C. Vigny, N. Chamotrooke, W. Simons, C. Rangin, and B. Ambrosius (2006), India and Sunda plates motion and deformation

along their boundary in Myanmar determined by GPS, *J. Geophys. Res.*, *111*, B05406, doi:10.1029/2005JB003877.

Subarya, C., M. Chlieh, L. Prawirodirdjo, J. P. Avouac, Y. Bock, K. Sieh, A. J. Meltzner, D. H. Natawidjaja, and R. McCaffrey (2006), Plate-boundary deformation associated with the Great Sumatra-Andaman earthquake, *Nature*, *440*, 46–51.

Tarantola, A. (2005), *Inverse Problem Theory and Methods for Model Parameter Estimation*, Soc. Indust. and Appl. Math., Philadelphia, Pa.

Yabuki, T., and M. Matsu'ura (1992), Geodetic data inversion using a Bayesian information criterion for spatial-distribution of fault slip, *Geophys. J. Int.*, *109*, 363–375.